Electronic Supplementary Material (ESI) for Journal of Materials Chemistry C.

Electronic Supplementary Information

Lattice dynamics in chiral tellurium by linear and circularly polarized Raman spectroscopy: crystal orientation and handedness

*Davide Spirito, Sergio Marras, Beatriz Martín-García**

Etching process for handedness determination

Fig. S1 shows the optical microscope images collected in the five bulk Te crystals studied after 30 min of etching with sulfuric acid at 100ºC. From the shapes and orientation of the etch pit formed in the (1 0 0) plane,[1] we determined the handedness of the five crystals.

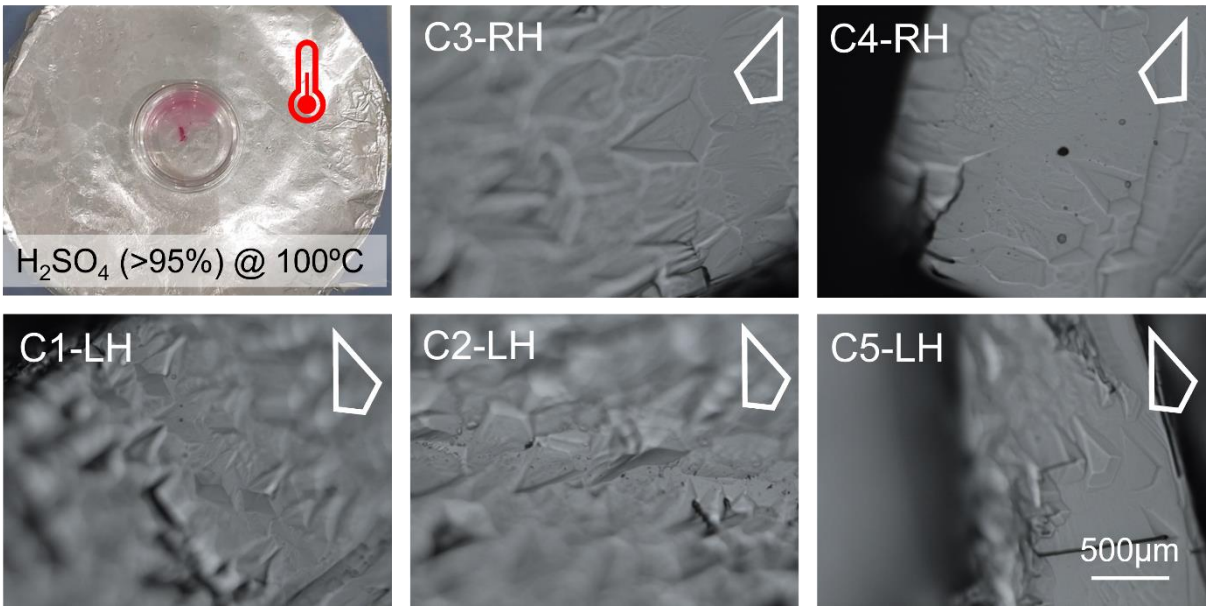

Fig. S1. Photograph collected during the etching process together with the corresponding etch pits images for the bulk Te crystals under study for the handedness determination.

Control experiments

Before carrying out the complete Raman spectroscopy characterization of the bulk Te crystals, we checked the acquisition conditions to avoid the formation of TeO_2,[2] which could modify the results since it presents modes at 120 and 140 cm^{-1} (**Fig. S2**) or Raman bands shift or broadening[3]. Moreover, we also confirmed that by lowering the temperature the Te Raman modes just systematically shift towards higher frequencies and narrower linewidth (**Fig. S3**).

The latter being relevant for a more reliable determination of the E modes shift (≤ 1 cm^{-1}) in the circular and helicity Raman measurements.

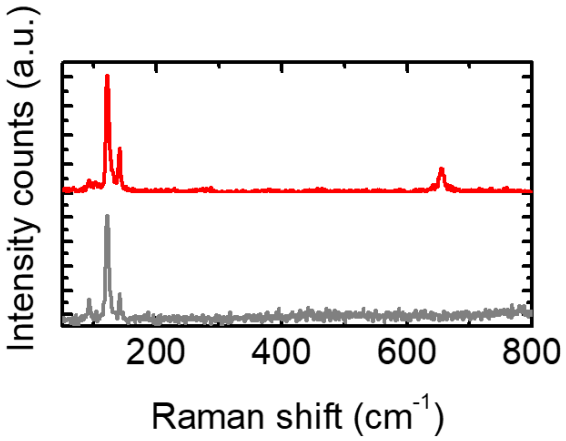

Fig. S2. Raman spectra acquired at different laser power: for > 1 mW (red line) a peak at 650 cm^{-1} appears and the relative intensity ratio between the 120 and 140 cm^{-1} modes changes due to the formation of TeO_2[2] and for < 1 mW (grey line).

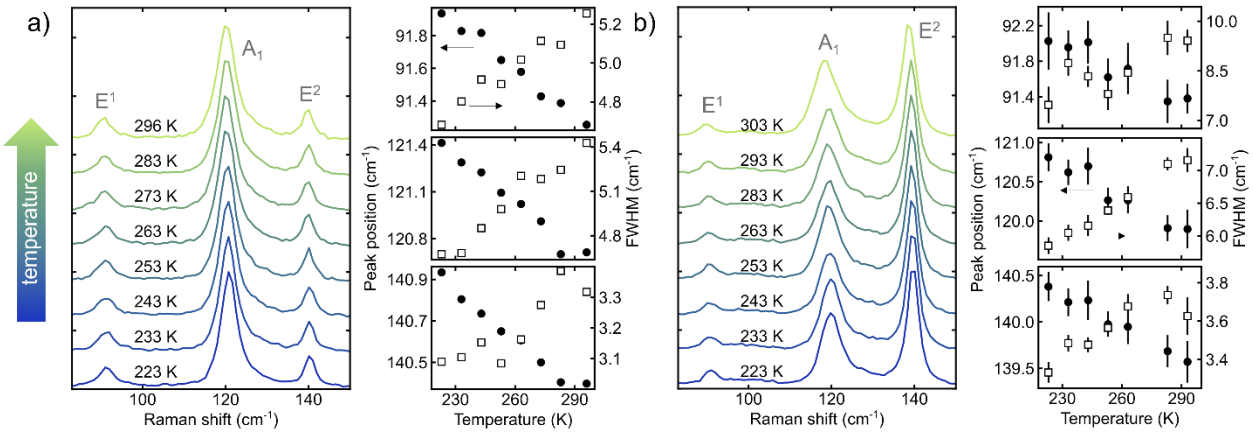

Fig. S3. Representative Raman spectra collected in two bulk Te crystals (a, b) at selected temperatures in the range (223-303K) with the three characteristic modes: E^1, A_1 and E^2. The temperature evolution of the modes position (full symbols) and linewidth (FWHM, empty symbols) is also displayed showing just a systematic shift towards higher frequencies and narrower linewidth when cooling down.

Additionally, to check the different optical set-ups implemented in the micro-Raman instrument, we carried out polarization tests using as a reference Si (100). The corresponding polar plots obtained in the parallel and cross configurations show the expected four loops and

a 45º shift between them (**Fig. S4**). In the case of the circular and helicity configurations, we confirmed that there is no shift in the main Si mode at 520.5 cm^{-1} under R/L and RL/LR settings (**Fig. S5**).

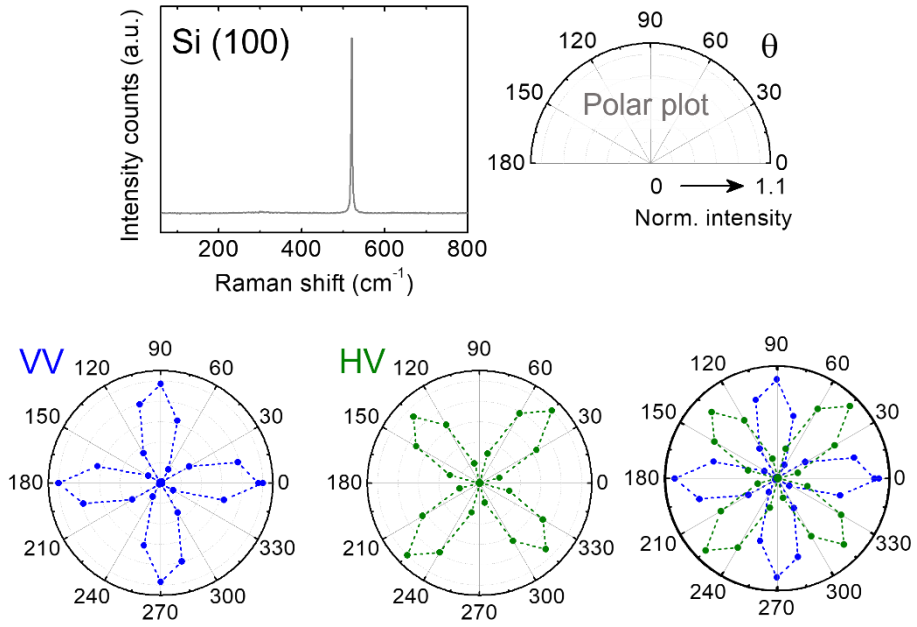

Fig. S4. Checking the angle-dependent linearly polarized Raman set-up by collecting the signal from Si (100) using the two configurations: parallel (VV) and cross (HV).

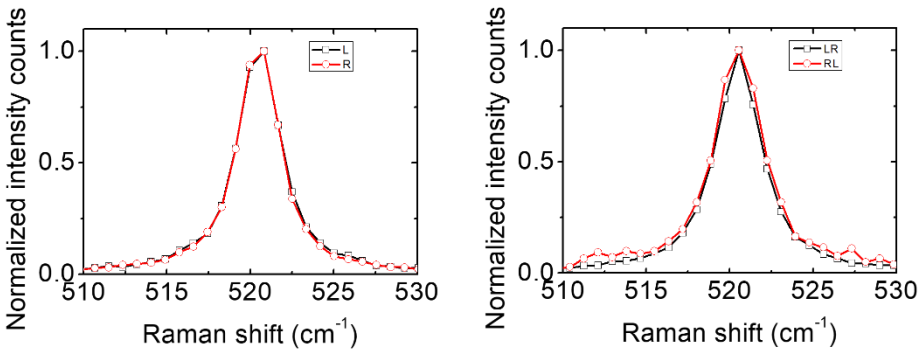

Fig. S5. Checking the circular polarization and helicity Raman set-up by collecting the signal from Si (100) using the different configurations used in this study and observing no shift in the main mode at 520.5 cm^{-1} under R/L and RL/LR settings.

Crystallographic planes layout

Fig. S6 shows the arrangement of the crystallographic planes accessible in the Te bulk crystals used in this work as well as the small difference in position of the (1 2 0) plane regarding (1 1 0) plane.

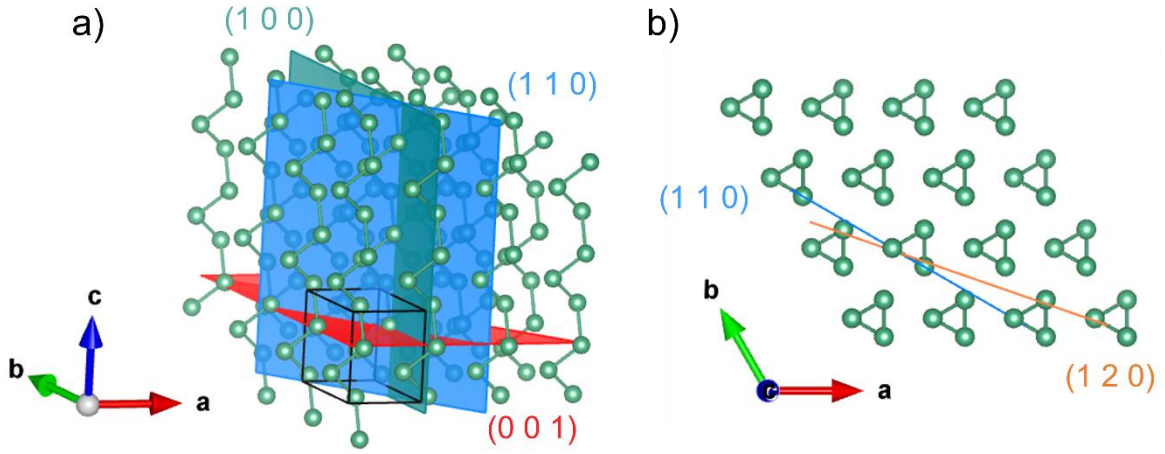

Fig. S6. Sketches drawn using the crystallographic data of Adenis *et al.*[4] for a right-handed structure (space group – $P3_121$) with Vesta software[5] showing: a) the layout of the crystallographic planes understudy and b) the small angle difference (~10 degrees) between planes (1 1 0) and (1 2 0).

Angle-dependent linearly polarized Raman spectroscopy in cross configuration

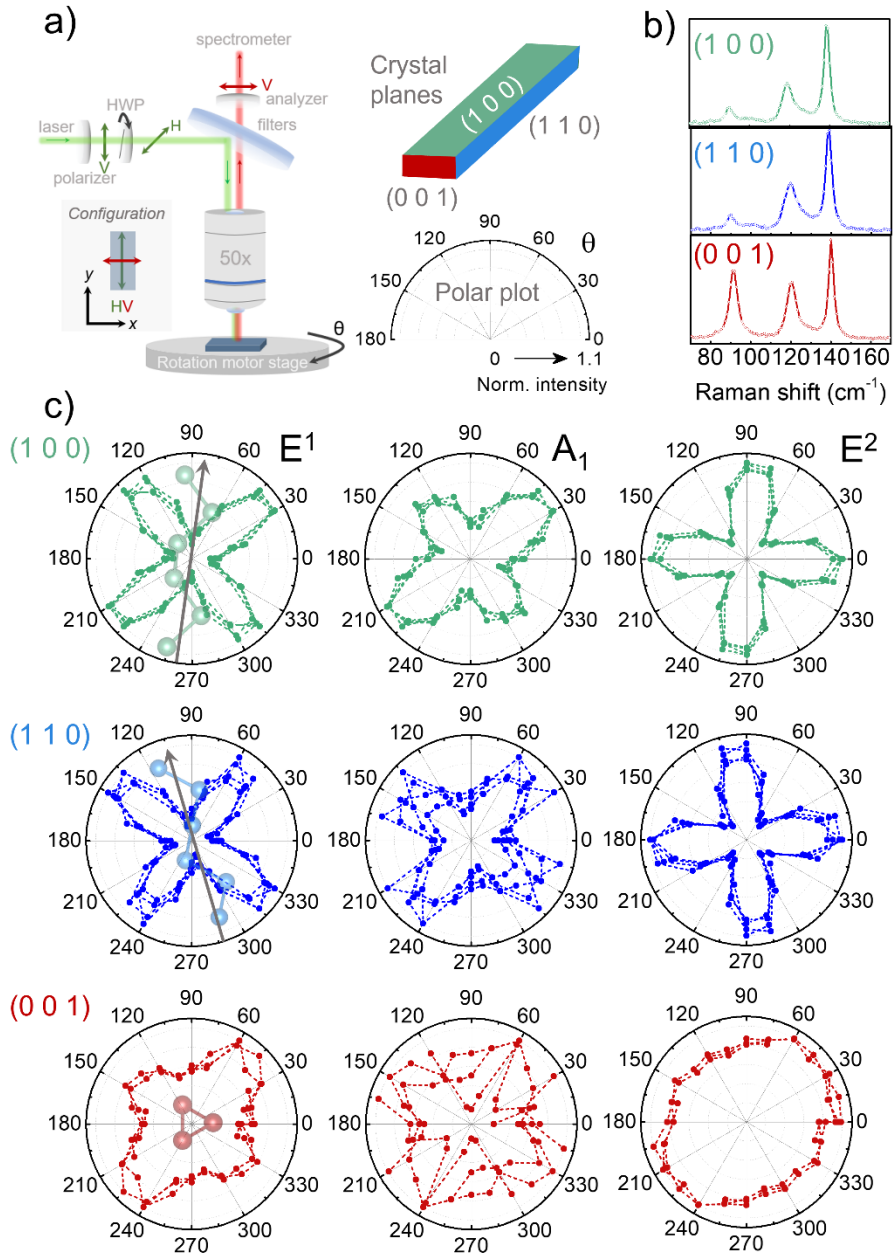

Fig. S7. Angle dependence of the phonon modes of the bulk Te crystals collected in cross (HV) configuration in the three different faces: a) Sketch of the angle-dependent linearly polarized Raman measurements showing the optical elements for this configuration, scale of the polar plots elaborated from the data obtained by rotating the Te bulk crystals (θ) and collecting signal for each plane (color-code) under study. b) Integrated Raman spectra along the polarization angle for the different planes studied. c) Normalized polar plots of the three Raman modes intensities (dots) extracted from the corresponding Raman spectra data in at least three different regions of the images shown in Fig. 2 (in C1 & C3). The orientation of the

polar plots and optical images (Fig. 2) are the same, no correction to the rotation angle (θ) has been made.

Raman tensor analysis: linearly polarized Raman and crystallographic planes

The analysis of Raman modes' intensity with varying linear polarization configuration is based on the theory of Raman tensors. For the point group of Te (D_3, 32) they are given by:

$$A_1 = \begin{bmatrix} a & 0 & 0 \\ 0 & a & 0 \\ 0 & 0 & b \end{bmatrix}, E(x) = \begin{bmatrix} c & 0 & 0 \\ 0 & -c & d \\ 0 & d & 0 \end{bmatrix}, E(y) = \begin{bmatrix} 0 & -c & -d \\ -c & 0 & 0 \\ -d & 0 & 0 \end{bmatrix}$$

The reference frame for the tensors is the standard one from the Volume A of International Tables for Crystallography (ITA),[6] so that the z-axis is aligned with the trigonal axis (*c*-axis).

The intensity of the Raman mode is then given $\propto |e_i R e_s|$, with R the Raman tensor, $e_{i,s}$ the incident and scattered polarization. For the case of degenerate modes (such as the E modes with E(x) and E(y) components) the sum of their intensity is considered. Here we consider a simplified model, and assume that the two components of E always have the same *c,d* coefficients. Additionally, we assume all the coefficients to be real.

Following the experimental conditions as described in the main text, we consider a backscattering geometry with incidence on different crystallographic planes. The sample is mounted so that the *z* direction in the laboratory frame is aligned with the normal to a specific plane, and the linear polarizations $e_{i,s}$ lie in this plane (*xy* plane in the lab reference frame), as shown in **Fig. S8**. The alignment of the reference frame of the laboratory and that of the crystal is a critical task in the derivation of the theoretical formulae for angular dependence and will be discussed in the following. The sample is rotated around the normal by an angle θ - theta, and the incidence and scattered polarization where selected to be parallel or perpendicular to each other (VV or HV configuration), and defined by polarization vector given by V and H.

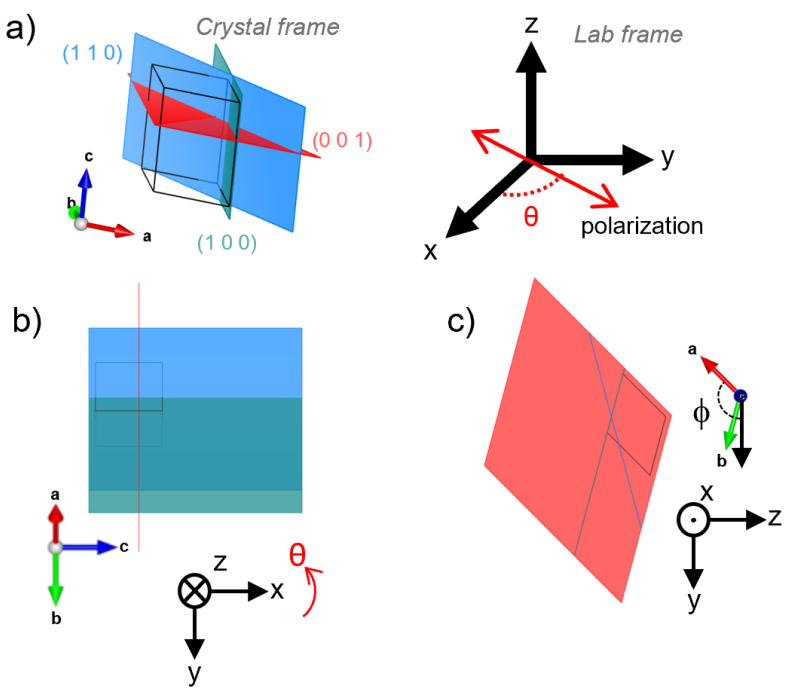

Fig. S8. a) Sketch of the crystal reference frame (*abc*) and laboratory frame (*xyz*). In the crystal the unit cell is marked. Colored crystallographic planes are (0 0 1) (red), (1 0 0) (green), (1 1 0) (blue). b,c) Alignment between crystal and reference frame, in two projections. The angles θ and φ defined in the text are shown.

The purpose of this analysis is to associate the characteristic patterns observed in the angular dependence with the alignment of the crystal. Furthermore, it will be possible to estimate the coefficients *a,b,c,d*, which allows to calculate Raman peak intensity in every orientation or polarization configuration. To make the rotations and modifications in the Raman tensors easier to follow, we start with the (0 0 1) plane whose analysis is simpler than the (1 0 0) and (1 1 0) planes.

Incidence along the trigonal c-axis (0 0 1 plane)

This case can be discussed directly using the Raman tensors reported above, without further rotation. The polarization vectors are thus V = (cosθ, sinθ, 0) and H = (sinθ¸ -cosθ, 0).

The A_1 mode will be thus proportional to the identity matrix, obtaining a constant intensity (proportional to a^2) in the VV configuration and null in HV. This is indeed observed experimentally, as reported in **Fig. S9**.

For the sum of E modes, both VV and HV have constant, non-null intensity (proportional to c^2), as verified experimentally.

From this calculation it is evident that the incidence along *z* is not sufficient to determine the direction of any of the crystal axes, nor the coefficients *a,b,c,d*.

Finally, we observe a slight deviation from theory, which can be ascribed to the incidence direction non-perfectly aligned with the *c*-axis. This occurs because of the mounting of the bulk crystals.

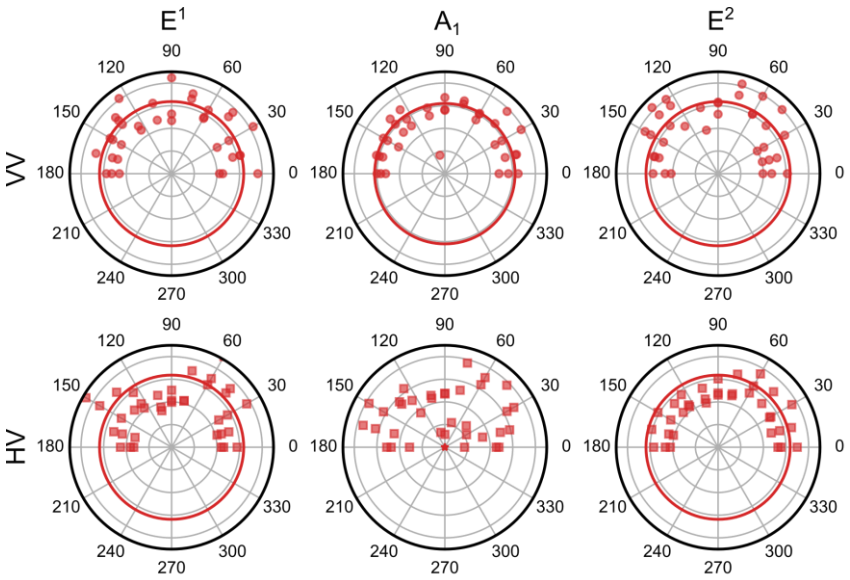

Fig. S9. Polar plots of the linear polarization angular dependence, for incidence along the helical chains (*c*-axis direction). Data are normalized as described in the text.

Incidence perpendicular to the trigonal c-axis (1 0 0 and 1 1 0 planes)

In this case, a rotation of the reference frame is needed to align the polarization in the *xyz* frame of the lab to that of the crystal. Before deriving the suitable rotation matrices, we discuss a more general formalism that allows to derive some important features of the angular pattern.

To this aim, we define the polarization vectors as $V = (\sin\vartheta \cos\varphi, \sin\vartheta \sin\varphi, \cos\vartheta)$ and $H = (\cos\vartheta \cos\varphi, \cos\vartheta \sin\varphi, \sin\vartheta)$. In this way, when the azimuth angle ϑ is 0, the polarization V is aligned with the *c*-axis. The angle φ defines the incidence with respect to the [100] direction (the calculation of φ is described above). Thus, the vectors V, H can be used for a family of incidence directions perpendicular to the trigonal axis.

We first consider the A_1 mode. In this case, the VV and HV patterns simplify as

$$I_{VV}^{A1}(\theta) = [(a-b)^2 \sin^2\theta + b]^2$$

$$I_{HV}^{A1}(\theta) = \frac{(a-b)^2}{4}\sin^2\theta$$

These functions are independent of ϕ. The VV case features an ellipsoid with axes aligned to $\vartheta=0$ and $\vartheta=\pi/2$. For $(b/a)^2<1$, the minor axis will be aligned with the *c*-axis. For $(b/a)^2>1$, the minor axis is perpendicular to the *c*-axis. In HV case, a pattern with four maxima is always observed, with its zeros aligned with $\vartheta=0, \pi/2$.

For the E modes, we first note that independently of *c,d* and φ, in the VV configuration with polarization aligned with the *c*-axis, the intensity is 0. This can be derived directly from the tensors shown above with $e_i=e_s=(0,0,1)$.

Considering the data in **Fig. S10**, we can identify the *c*-axis as close to π/2 (dashed line) finding the zero of the E modes in VV configuration.

The two modes E^1 and E^2 have a clearly different pattern, depending on the relative value of *d/c*.

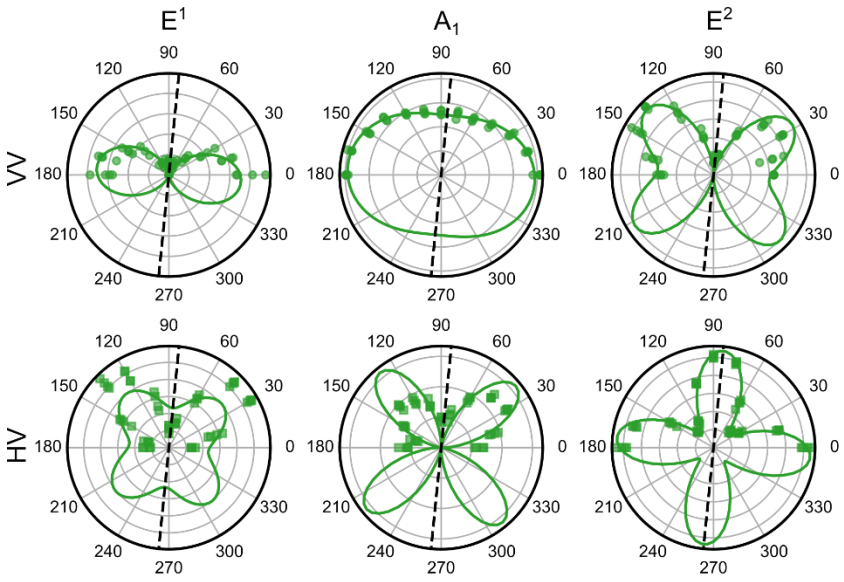

Fig. S10. Polar plots of the linear polarization angular dependence, for incidence in the (1 0 0) plane. Data are normalized as described in the text. Black lines are best fit to the data. Dashed lines mark the direction of the *c*-axis.

The general angular dependence is given by:

$$I_{VV}^{E}(\theta,\phi) = c^2\sin^4(\theta) - 16cd\sin^3(\phi)\sin^3(\theta)\cos(\theta) + 12cd\sin(\phi)\sin^3(\theta)\cos(\theta) + 4d^2\sin^2(\theta)\cos^2(\theta)$$

$$I_{HV}^{E}(\theta,\phi) = \frac{(c\cos(\phi-2\theta) - c\cos(\phi+2\theta) + 2d\cos(2\theta))^2\cos^2(\phi)}{4} + \left(2c\sin^2(\phi)\sin(\theta)\cos(\theta) - \frac{c\sin(2\theta)}{2} + 2d\sin(\phi)\sin^2(\theta) - d\sin(\phi)\right)^2$$

Before discussing the features of these patterns, we discuss the determination of the angle φ and how to deal with equivalent planes.

Direction of incidence and determination of the angle ϕ

The procedure to obtain the Raman intensity for arbitrary orientation of the crystal requires the rotation matrix $C_{lab->crystal}$ to convert between the two reference frames. Then, the intensity is $\propto \left|e_i C_{lab->crytsal}^{T} R C_{lab->crystal} e_s\right|^2$.

The formalism described above simplified this procedure for the special cases of polarization parallel or perpendicular to the *c*-axis. In the case parallel to the *c*-axis, no rotation is needed. Considering the case of the polarization perpendicular to the *c*-axis, the matrix can be found by imposing that (see also Fig. S8):

1. The lab direction *x* is parallel to the *c*-axis of the crystal.
2. The lab direction *z* is parallel to the incidence direction *n*.
3. The direction *n* must be selected considering the hexagonal symmetry of the Te lattice. In particular, we note that the [100] direction is not parallel to the normal of the (1 0 0) plane.
4. The 3rd base vector of the rotated system is then found by the cross product of *n* and the direction [001].
5. The ϕ is given by the director cosines of this last base vector. In particular, we find:
    a. ϕ=- $\pi/3$ for incidence along the normal to (1 0 0)
    b. ϕ=- $\pi/6$ for incidence normal to (1 1 0), and $\phi=\pi/6$ for incidence normal to (-1-10)

Equivalent planes

When the Raman incidence occurs on equivalent planes their contribution must be added. This is required for the E modes, as the A_1 patterns are independent of ϕ.

Considering thus only the E modes, for planes with ϕ*=0, ±π/3…*, positive and negative ϕ yield the same patterns, so calculating the case ϕ=0 is sufficient. For the case of (1 1 0) and (-1 -1 0), that have opposite values of ϕ, ϕ*=-π/6* and ϕ*=π/6*, the two patterns are shift by π/3, as shown in the **Fig. S11**. For the calculation of intensity, the sum matches that of ϕ=0, as can be shown from the equations reported above.

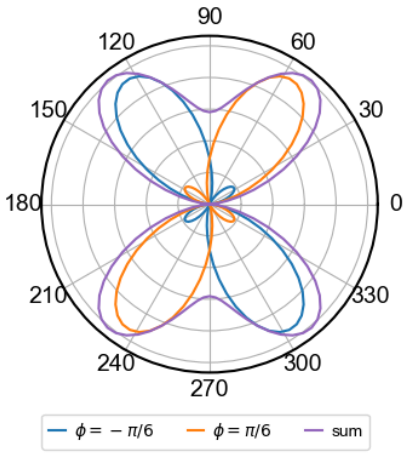

Fig. S11. Expected polar plot for the E modes with *d/c*=1.2 for ϕ*=-π/6* and ϕ*=π/6* (blue and orange line) and for their sum (purple line).

Analysis of the angle-dependence for E modes

The values of the ratio *d/c* for the E modes can be estimated from the shape of the linear polarization pattern.

The number of maxima of the VV pattern will give an indication of the ratio *d/c*. For $(d/c)^2>1/2$, there will be four maxima at angle different from 0, π/2. For $(d/c)^2<1/2$, only 2 maxima are found at π/2. Looking at the figure, the E^1 (with 2 maxima) and E^2 (with 4 maxima) are clearly different.

Also from the analysis of the HV functions, we can derive further information about the magnitude of *c,d*. The maximum or minimum of the HV curve is aligned to the *c*-axis according to the following conditions:

- if $(d/c)^2<1/4$, the zero in VV corresponds to a minimum in HV
- if $(d/c)^2>1/4$, the zero in VV corresponds to a minimum in HV

From the data in the Fig. S10, referring to the plane labeled (1 0 0), we find that the minimum in HV of the E^2 mode is aligned with the zero in VV, indicating that $(d/c)^2>1/4$; for the E^1 mode, the zero in VV matches a minimum in HV, so that for this mode $(d/c)^2<1/4$.

In summary, when the polarization is incidence is normal to the *c*-axis, we can observe the following in the angular dependence:

- For the E modes, the VV has a zero when the polarization is aligned with the helical chains laying along the *c*-axis.
- For the A_1 modes, the maxima or minima are aligned with the *c*-axis, depending on the *b/a* ratio.
- The number of maxima the VV pattern of the E modes depends on the *d/c* ratio.
- For both A_1 and E modes, the HV has a π/2 periodicity in θ.
- For the E modes, the HV will have a maximum or a minimum aligned with the *c*-axis depending on the *d/c* ratio.
- For the E modes, the same pattern is expected for incidence normal to the *c*-axis, since the sum $I(\vartheta,\phi)+ I(\vartheta,-\phi)=2\, I(\vartheta,\phi=0)$ must be considered. The formulas are thus:

$$I_{VV}^{E}(\theta) = c^2 \sin^4(\theta) + 4d^2 \sin^2(\theta)\cos^2(\theta)$$
$$I_{HV}^{E}(\theta) = c^2 \sin^2(\theta)\cos^2(\theta) + d^2 \cos^2(2\theta)$$

This analysis can be applied to all the crystals whose point group is D_3 (32) or others with the same form of the Raman tensors, i.e. C_{3v} (3m) and D_{3d} (-3m).

Fitting procedure

The measured intensity of the Raman mode depends on the polarization selection rules, as discussed above, as well as on experimental factors such as laser wavelength or temperature. Therefore, the absolute determination of the coefficients in the Raman tensors is not possible. However, for the case of A_1 and E modes as above, we can evaluate the ratios *b/a* and *d/c*.

To this aim, we have analyzed the angular dependent data after normalization by the integral of the intensity as a function of θ between 0 and π. These integrals of both VV and HV are given by:

$$S_{VV}^{A1} = \frac{\pi}{8}(3a^2 + 3b^2 + 2ab), S_{HV}^{A1} = \frac{\pi}{8}(a-b)^2$$
$$S_{VV}^{E} = \frac{\pi}{8}(3c^2 + 4d^2), S_{HV}^{E} = \frac{\pi}{8}(c^2 + 4d^2)$$

As discussed before, the same pattern is expected for all the cases when the incidence is perpendicular to the *c*-axis. This is indeed observed in **Figs.** S10 and **S12**, relative to the planes (1 0 0) and (1 1 0).

We extract the values of the ratios *b/a* and *d/c* using the formulas above in VV and HV. The results of the fitting procedure for the (1 0 0) plane is shown in Fig. S6. The coefficients *b/a* and *c/d* are reported in **Table S1** below obtained from the Raman measurements carried out in several crystals.

For the plane (1 1 0), the pattern is well reproduced by the same *d/c* and *b/a* values as in the (1 0 0) plane, as shown in Fig. S8.

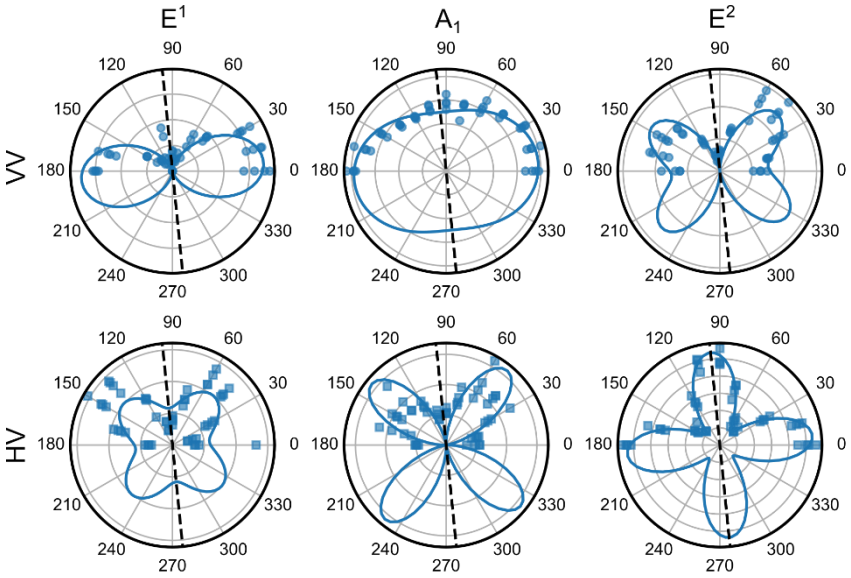

Fig. S12. Polar plots of the linear polarization angular dependence, for incidence in the (1 1 0) plane. Data are normalized as described in the text. Dashed lines mark the direction of the trigonal axis.

Additionally, in the configuration with incidence parallel to the *c*-axis, we can obtain the ratio *c/a* directly from the data in VV configuration; the same value can be obtained using the ratio of $I_{VV}(\theta)$ for the perpendicular direction. The values are reported in Table S1.

Table S1. Coefficients of the Raman tensors extracted from angular dependence of linearly polarized Raman.

Mode	b/a	c/d	c/a	d/a
E^1 (90 cm^{-1})		0.3-0.4	~0.4	~0.1
A_1 (120 cm^{-1})	0.8-0.85			
E^2 (140 cm^{-1})		1.1-1.2	~0.5	~0.6

Circularly polarized Raman spectroscopy measurements in the (1 0 0) and (1 1 0) planes

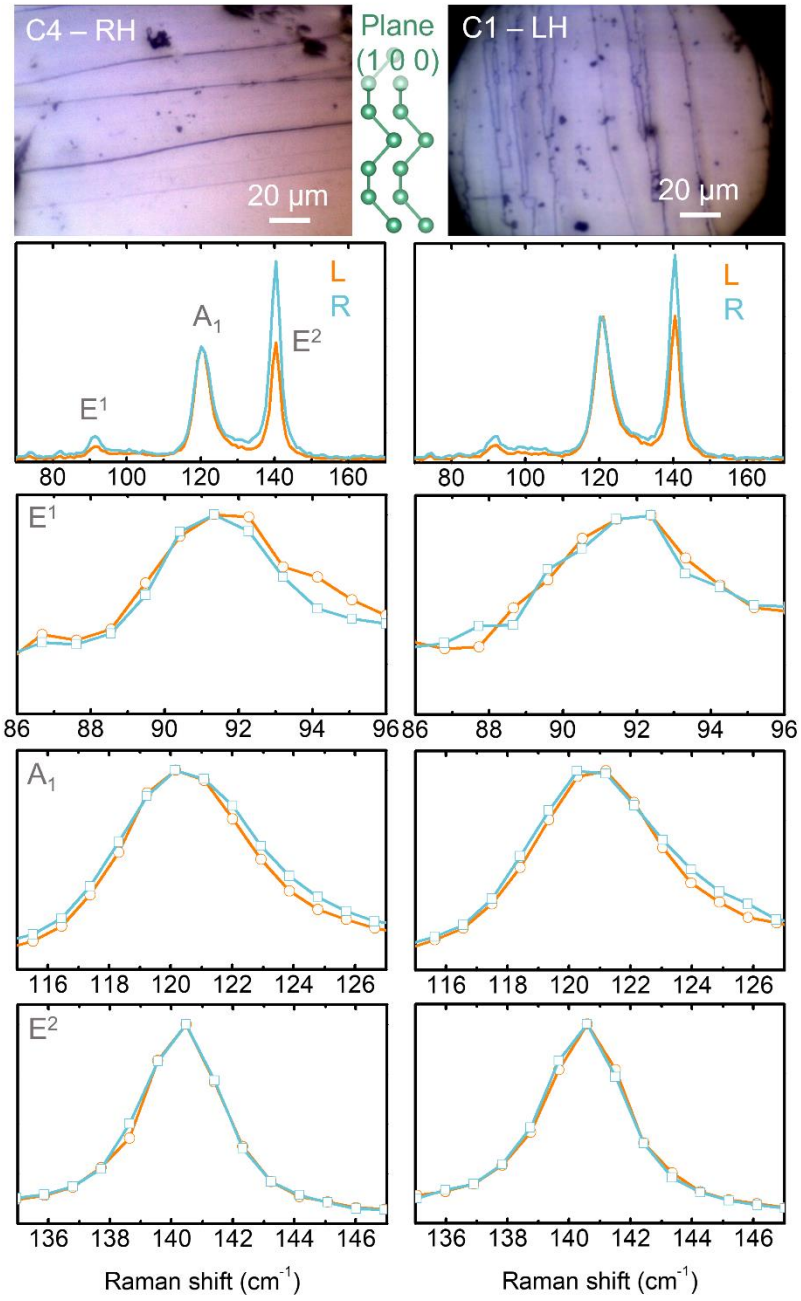

Fig. S13. Circularly polarized Raman characterization of representative right- and left-handed bulk Te crystals (C4, C1) carried out falling upon the (1 0 0) crystallographic plane, and using incident circularly polarized light and collecting unpolarized signal: Optical images taken with the micro-Raman instrument of the crystal faces under study accompanied by representative Raman spectra showing the characteristic Raman modes (E^1, A_1 and E^2) obtained using right- and left-handed light excitation (below). The panels below present zoomed ranges of the normalized Raman spectra showing no shift in any of the E or A_1 phonons.

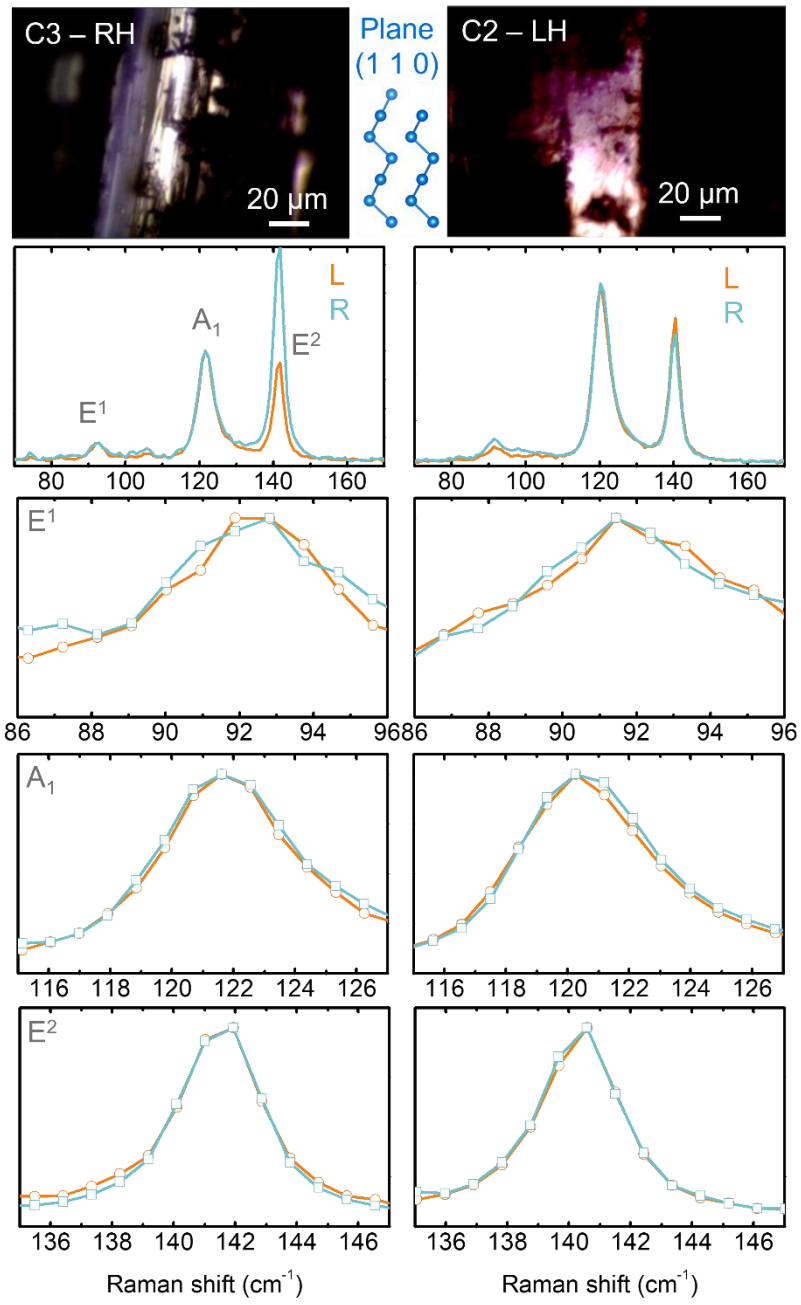

Fig. S14. Circularly polarized Raman characterization of representative right- and left-handed bulk Te crystals carried out falling upon the (1 1 0) crystallographic plane, and using incident circularly polarized light and collecting unpolarized signal: Optical images taken with the micro-Raman instrument of the crystal faces under study accompanied by representative Raman spectra showing the characteristic Raman modes (E^1, A_1 and E^2) obtained using right- and left-handed light excitation (below). The panels below present zoomed ranges of the normalized Raman spectra showing no shift in any of the E or A_1 phonons.

Helicity resolved Raman spectroscopy measurements in the (1 0 0) and (1 1 0) planes

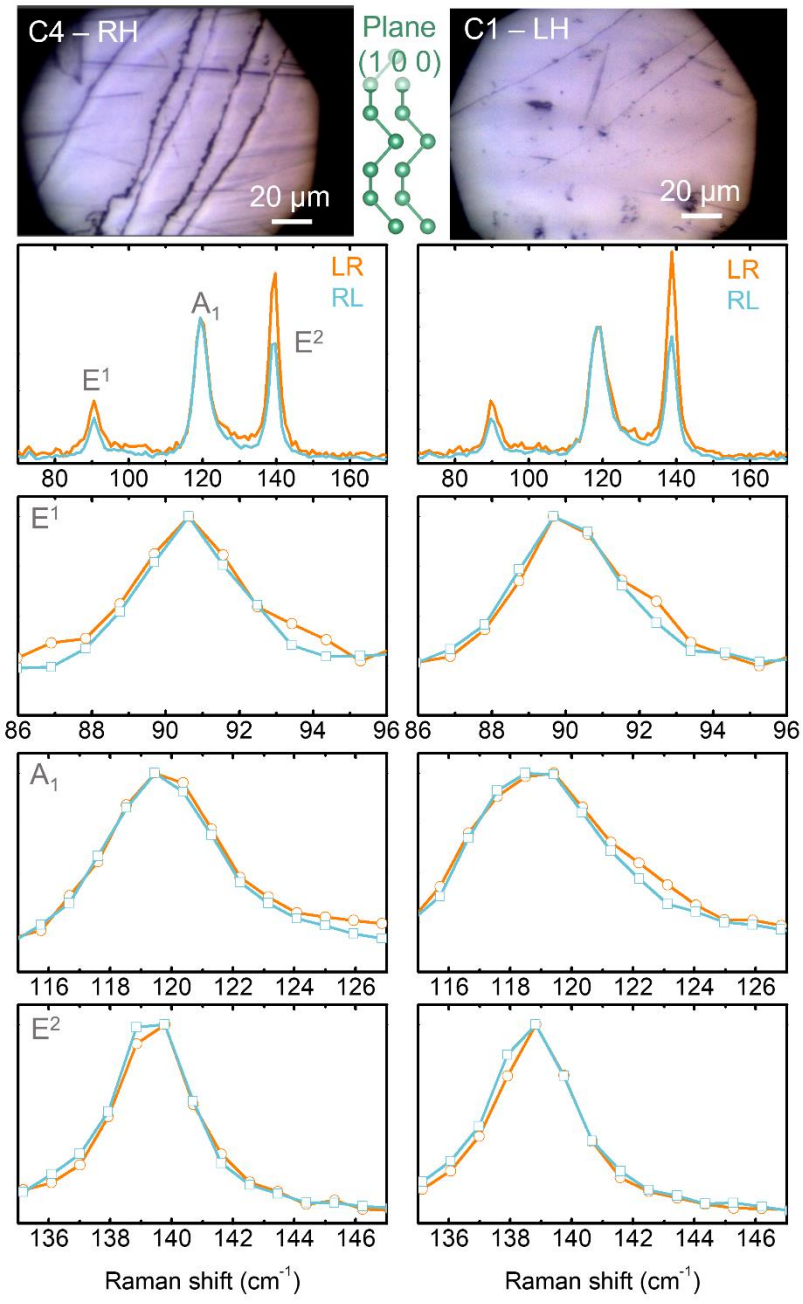

Fig. S15. Helicity-resolved Raman spectroscopy characterization of representative right- and left-handed bulk Te crystals (C4, C1) carried out falling upon the (1 0 0) crystallographic plane and using incident and collected circularly polarized light with contrary handedness: LR & RL. Optical images taken with the micro-Raman instrument of the crystal faces under study accompanied by representative helicity-resolved Raman spectra showing the characteristic

Raman modes (E^1, A_1 and E^2) obtained using the two configurations: LR & RL. The panels below present zoomed ranges of the normalized Raman spectra showing no shift in any of the E or A_1 phonons.

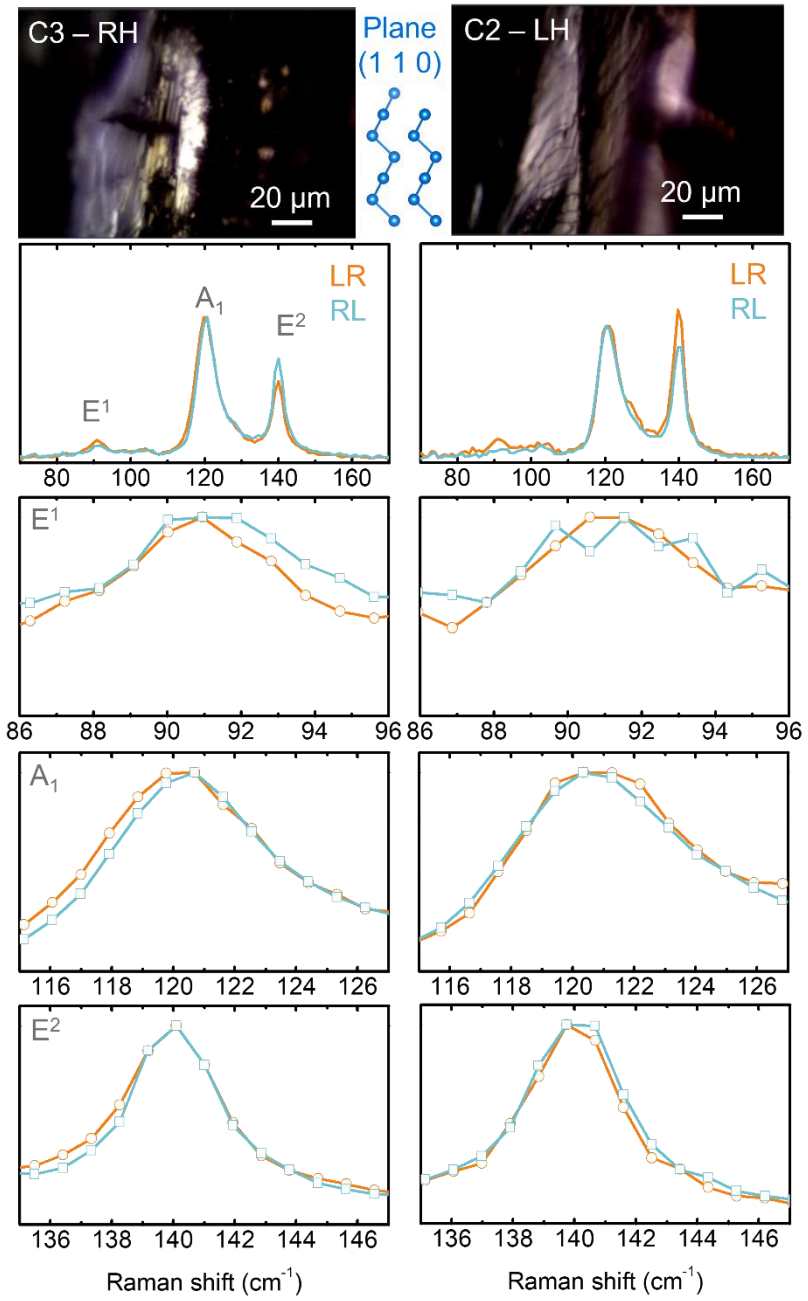

Fig. S16. Helicity-resolved Raman spectroscopy characterization of representative right- and left-handed bulk Te crystals carried out falling upon the (1 1 0) crystallographic plane and using incident and collected circularly polarized light with contrary handedness: LR & RL. Optical images taken with the micro-Raman instrument of the crystal faces under study accompanied

by representative helicity-resolved Raman spectra showing the characteristic Raman modes (E^1, A_1 and E^2) obtained using the two configurations: LR & RL. The panels below present zoomed ranges of the normalized Raman spectra showing no shift in any of the E or A_1 phonons.

Table S2. Statistics of the shift of the E modes in the (0 0 1) plane using different circularly polarized Raman configurations in the five bulk Te crystals under study with incident light parallel to the *c*-axis.

Crystal	Points measured	E^1 mode shift (cm^{-1})	E^2 mode shift (cm^{-1})	Configuration
C1-LH	44	0.58±0.09	0.14±0.28	R/- & L/-
	30	0.87±0.08	0.22±0.18	RL & LR (PAM)
C2-LH	98	0.61±0.08	0.19±0.07	R/- & L/-
	12	0.81±0.09	0.23±0.11	RL & LR (PAM)
C3-RH	64	-0.54±0.08	-0.10±0.06	R/- & L/-
	28	-0.86±0.09	-0.18±0.05	RL & LR (PAM)
C4-RH	53	-0.49±0.11	-0.07±0.06	R/- & L/-
	33	-0.79±0.15	-0.16±0.05	RL & LR (PAM)
C5-LH	57	0.51±0.25	0.14±0.26	R/- & L/-
	12	0.93±0.07	0.27±0.07	RL & LR (PAM)

Table S3. Statistics of the shift of the E modes in the (1 0 0) plane using different circularly polarized Raman configurations in several bulk Te crystals under study.

Crystal	Points measured	E^1 mode shift (cm^{-1})	E^2 mode shift (cm^{-1})	Configuration
C1-LH	47	-0.43±0.38	0.04±0.11	R/- & L/-
	8	0.21±0.17	0.05±0.06	RL & LR (PAM)
C2-LH	19	-0.52±0.53	0.07±0.10	R/- & L/-
	12	-0.35±0.88	0.23±0.12	RL & LR (PAM)
C3-RH	11	0.34±0.77	0.07±0.05	R/- & L/-
	16	-0.10±0.23	0.03±0.23	RL & LR (PAM)
C4-RH	8	0.29±0.34	0.06±0.03	R/- & L/-
	5	0.01±0.07	0.10±0.04	RL & LR (PAM)
C5-LH	8	-0.06±0.33	0.03±0.03	R/- & L/-
	12	0.77±0.88	0.01±0.09	RL & LR (PAM)

Table S4. Statistics of the shift of the E modes in the (1 1 0) plane using different circularly polarized Raman configurations in several bulk Te crystals under study.

Crystal	Points measured	E^1 mode shift (cm^{-1})	E^2 mode shift (cm^{-1})	Configuration
C2-LH	35	-0.65±0.81	0.01±0.29	R/- & L/-
	12	-0.90±1.28	-0.10±0.16	RL & LR (PAM)
C3-RH	48	-0.30±1.11	0.18±0.33	R/- & L/-
	12	0.71±1.05	-0.02±0.16	RL & LR (PAM)

References:

1 A. Koma and S. Tanaka, *phys. stat. sol. (b)*, 1970, **40**, 239–248.

2 I. Rosina, B. Martín-García, D. Spirito, Z. Dang, G. Gariano, S. Marras, M. Prato, R. Krahne, L. De Trizio and L. Manna, *Chem. Mater.*, 2020, **32**, 2978–2985.

3 V. V. Poborchii, V. A. Sachkov, A. A. Shklyaev, A. V. Fokin and P. I. Geshev, *Journal of Physics and Chemistry of Solids*, 2024, **185**, 111806.

4 C. Adenis, V. Langer and O. Lindqvist, *Acta Crystallogr C Cryst Struct Commun*, 1989, **45**, 941–942.

5 K. Momma and F. Izumi, *Journal of Applied Crystallography*, 2011, **44**, 1272–1276.

6 M. I. Aroyo, Ed., *International Tables for Crystallography: Space-group symmetry*, International Union of Crystallography, Chester, England, 2nd edn., 2016, vol. A.